Conserved salt-bridge competition triggered by phosphorylation regulates the protein interactome

John J. Skinner[a,b,1,2], Sheng Wang[c,d,1,3], Jiyoung Lee[a], Colin Ong[a], Ruth Sommese[e], Sivaraj Sivaramakrishnan[e], Wolfgang Koelmel[f], Maria Hirschbeck[f], Hermann Schindelin[f], Caroline Kisker[f], Kristina Lorenz[g,h,i], Tobin R. Sosnick[b,4], and Marsha Rich Rosner[a,4]

[a]Ben May Department for Cancer Research, University of Chicago, Chicago, IL 60637; [b]Department of Biochemistry and Molecular Biology, Institute for Biophysical Dynamics, University of Chicago, Chicago, IL 60637; [c]Toyota Technological Institute at Chicago, Chicago, IL 60637; [d]Department of Genetics, University of Chicago, Chicago, IL 60637; [e]Department of Genetics, Cell Biology, and Development, University of Minnesota, Minneapolis, MN 55455; [f]Rudolf Virchow Center for Experimental Biomedicine, University of Würzburg, 97078 Würzburg, Germany; [g]Institute of Pharmacology and Toxicology, University of Würzburg, 97078 Würzburg, Germany; [h]Cardiovascular Pharmacology, Leibniz-Institut für Analytische Wissenschaften (ISAS), 44139 Dortmund, Germany; and [i]West German Heart and Vascular Center Essen, University Hospital Essen, 45122 Essen, Germany

Edited by Natalia Jura, University of California, San Francisco, CA, and accepted by Editorial Board Member Brenda A. Schulman November 10, 2017 (received for review June 27, 2017)

Phosphorylation is a major regulator of protein interactions; however, the mechanisms by which regulation occurs are not well understood. Here we identify a salt-bridge competition or "theft" mechanism that enables a phospho-triggered swap of protein partners by Raf Kinase Inhibitory Protein (RKIP). RKIP transitions from inhibiting Raf-1 to inhibiting G-protein–coupled receptor kinase 2 upon phosphorylation, thereby bridging MAP kinase and G-Protein–Coupled Receptor signaling. NMR and crystallography indicate that a phosphoserine, but not a phosphomimetic, competes for a lysine from a preexisting salt bridge, initiating a partial unfolding event and promoting new protein interactions. Structural elements underlying the theft occurred early in evolution and are found in 10% of homo-oligomers and 30% of hetero-oligomers including Bax, Troponin C, and Early Endosome Antigen 1. In contrast to a direct recognition of phosphorylated residues by binding partners, the salt-bridge theft mechanism represents a facile strategy for promoting or disrupting protein interactions using solvent-accessible residues, and it can provide additional specificity at protein interfaces through local unfolding or conformational change.

phospho-swap | protein interaction | salt-bridge competition | Raf Kinase Inhibitory Protein | conformational change

Phosphorylation is a ubiquitous posttranslational modification implicated in the regulation of innumerable processes (1). Phosphorylation often acts as a switch, controlling the formation of protein complexes that mediate function. However, beyond directly forming either favorable or unfavorable interactions at the binding interface, the possible modes of phospho-regulation are not clear (2, 3). Here, we investigate how phosphorylation of RKIP (PEBP1), a member of the phosphatidylethanolamine protein family, reorganizes a salt-bridge network to bring about a localized conformational change and an exchange of signaling partners. Bioinformatic analyses demonstrate the broader significance of this mechanism, which represents a general mechanism to regulate both homo-oligomeric and hetero-oligomeric protein interactions.

As a regulator of MAP kinase and G-Protein–Coupled Receptor (GPCR) signaling, RKIP prevents numerous pathological conditions including metastatic cancer (4–6) and heart disease (7, 8) (Fig. 1*A*). Well-characterized structurally by crystallography and NMR (9–11), RKIP assumes a highly conserved conformation with a pocket composed of a loop that interacts noncovalently with its C-terminal α-helix (Fig. 1*B*). Phosphorylation at S153 by protein kinase C (PKC) switches RKIP from binding Raf-1 to binding G-protein–coupled receptor kinase 2 (GRK2) (12–14), thus activating a new pathway (Fig. 1*A*).

To observe the effects of phosphorylating RKIP at S153 by NMR, we mixed the catalytic subunit of PKC with RKIP and analyzed the heteronuclear single quantum coherence (HSQC) spectra over 10 h. We also inserted a minimally perturbing P74L mutation shown previously to increase the phosphorylation rate of RKIP (10). Several lines of evidence indicate that phosphorylation, which had the proper mass shift (*SI Appendix*, Fig. S1), was nearly complete. These include the previously published result that only position S153 is phosphorylated by PKC (12–14) and a reduction in the S153 NMR peak height by greater than 80% (Fig. 2*A* and *SI Appendix*, Fig. S1).

Comparison of the NMR ^{1}H-^{15}N HSQC spectra of unphosphorylated and phosphorylated $RKIP^{P74L}$ revealed pronounced differences at more than one-third of the amide NH (NH) peaks (Fig. 2*A*). Changes included peak movement, line broadening, and disappearance of peaks for residues located near S153; however, these effects extended out to residues in the C-terminal helix located more than 30 Å away. These changes indicated that a subset of amide NHs experienced different chemical environments due to altered conformation(s), with some undergoing

Significance

Phosphorylation is a ubiquitous modification that has been implicated in signaling and other functions, but the atomic-level mechanisms are not completely understood. We identify a salt-bridge competition or "theft" mechanism wherein a phosphoserine, but not a phosphomimetic, breaks a pre-existing salt bridge, initiating a partial unfolding event and promoting new protein interactions. Structural elements underlying the theft occurred early in evolution and are found in 10% of homo-oligomers and 30% of hetero-oligomers. These findings identify a facile and evolutionarily accessible mechanism for reorganizing salt bridges and other electrostatic networks with only a single mutation to trigger a functional switch.

Author contributions: J.J.S., K.L., T.R.S., and M.R.R. designed research; J.J.S., S.W., J.L., C.O., W.K., M.H., H.S., and C.K. performed research and analyzed data; R.S., S.S., and K.L. contributed new reagents/analytic tools; J.J.S., S.W., T.R.S., and M.R.R. analyzed data; and J.J.S., T.R.S., and M.R.R. wrote the paper.

The authors declare no conflict of interest.

This article is a PNAS Direct Submission. N.J. is a guest editor invited by the Editorial Board.

Data deposition: The atomic coordinates and structure factors have been deposited in the RCSB Protein Data Bank, www.rcsb.org [PDB ID codes 6ENS (RKIP) and 6ENT (Δ143-146 variant)].

[1]J.J.S. and S.W. contributed equally to this work.

[2]Present address: iHuman Institute, ShanghaiTech University, Shanghai 201210, China.

[3]Present address: Computational Bioscience Research Center, King Abdullah University of Science and Technology, Thuwal 23955-6900, Saudi Arabia.

[4]To whom correspondence may be addressed. Email: trsosnic@uchicago.edu or m-rosner@uchicago.edu.

This article contains supporting information online at www.pnas.org/lookup/suppl/doi:10.1073/pnas.1711543114/-/DCSupplemental.

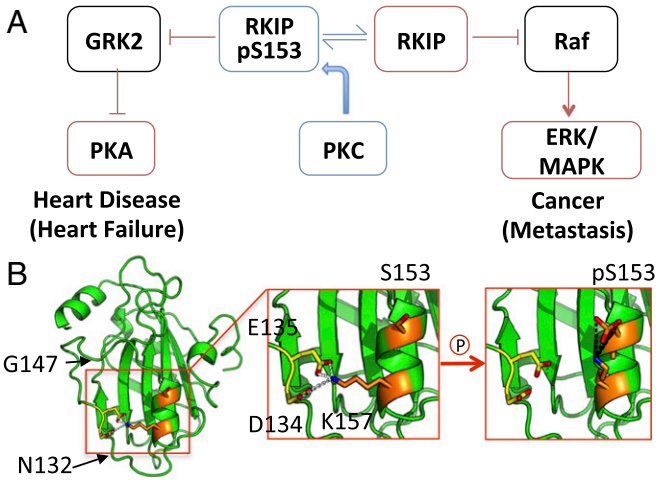

Fig. 1. RKIP function and structure. (*A*) Phosphorylation of S153 causes RKIP to inhibit GRK2 rather than Raf. RKIP acts to suppress heart disease and cancer. (*B*) Model of salt-bridge interactions and the proposed effects of S153 phosphorylation of RKIP. (*B*, *Left*) Key residues mapped onto the WT RKIP structure. (*B*, *Middle*) K157 interacts with D134-E135 in the WT RKIP crystal structure (yellow). (*B*, *Right*) A model of how pS153 could outcompete D134 and E135 for interaction with K157 (orange). Images were generated using PyMOL (The PyMOL Molecular Graphics System, Version 2.0, Schrödinger, LLC).

dynamical averaging between alternative conformations on the millisecond to microsecond timescale. An increase in the number of peaks in the random coil region (Fig. 2*A*, dashed circle) suggested a partial unfolding of residues 132–147 located in a well-folded loop region in the crystal structure. These findings indicated that the protein undergoes a large-scale perturbation upon PKC-induced phosphorylation of S153.

To probe the nature of the perturbation, we introduced mutations at or near S153. We first compared the HSQC spectrum of $RKIP^{pS153,P74L}$ to the phosphomimetic mutant $RKIP^{S153E}$. We showed previously that the $RKIP^{S153E}$ variant bound Raf-1 instead of GRK2, and its HSQC spectrum was nearly identical to that of wild-type (WT) RKIP (10). Consistent with these findings, the singly charged $RKIP^{S153E}$ was insufficient to induce the large-scale perturbation of the HSQC spectrum observed with the authentic phosphorylation of S153 (compare Fig. 2 *A* and *B*).

To investigate why the phosphomimetic was insufficient, we examined the RKIP structure and noted that K157, located one helical turn away from S153, could be involved in the phosphorylation-induced structural changes. In the crystal structure, K157 forms a salt bridge with D134 and E135 on a nearby loop (Fig. 1*B*). We posited that the K157 side chain, upon phosphorylation of S153, could rotate and form a salt bridge with the double charged phosphate on pS153. Such a rotation of K157 would leave the negatively charged ends of D134 and E135 near each other without a compensating positive charge. As a result, the acidic groups should have a tendency to separate, and the loop containing the two residues would become partially disordered.

Support for the ability of pS153, but not the S153E phosphomimetic, to outcompete residues D134 and E135 for K157 comes from peptide studies showing that the salt bridge formed between a phosphoserine and a lysine located at positions i and i+4 along a helix is unusually stable (~2 $kcal \cdot mol^{-1}$) relative to a standard K-E salt bridge (15). For RKIP, we propose that this

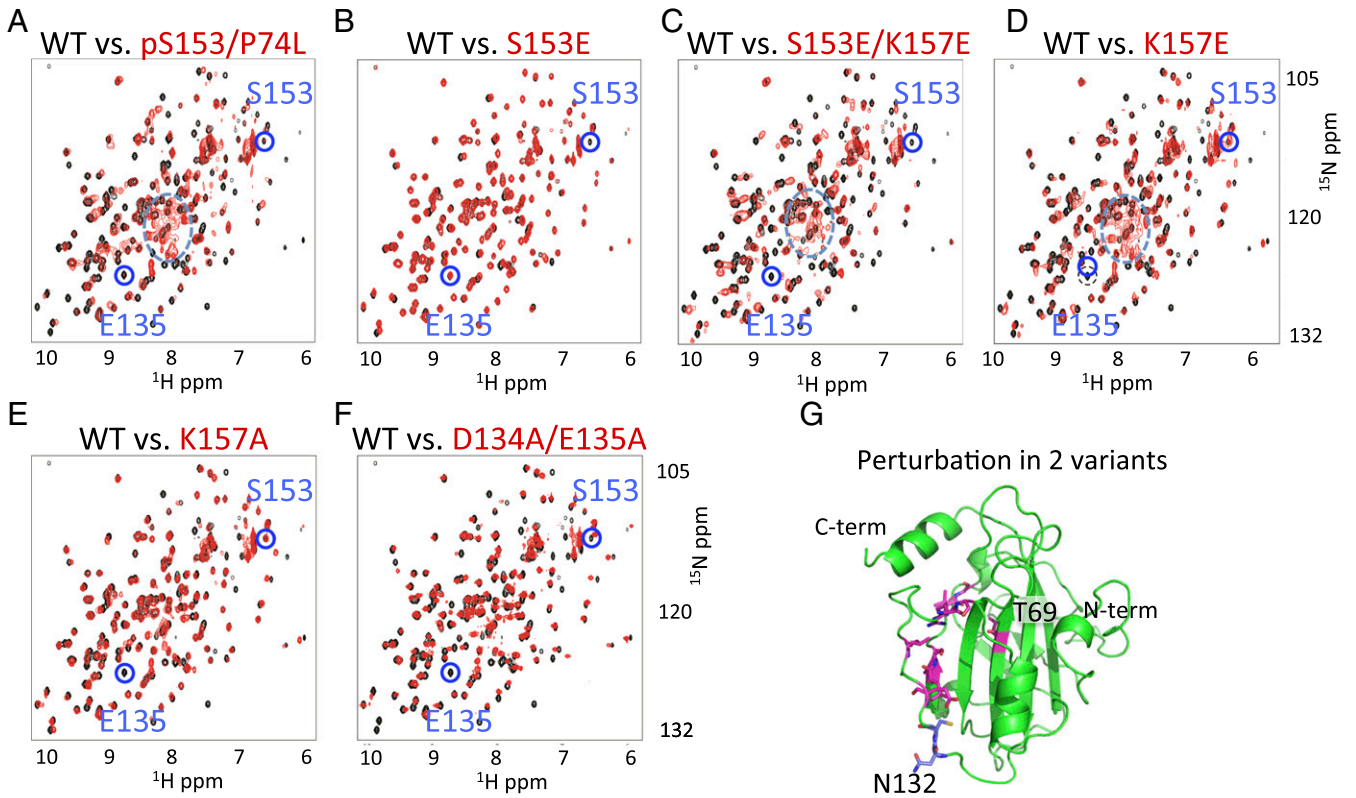

Fig. 2. ^{1}H-^{15}N HSQC NMR spectra. (*A*–*F*) Comparison of WT RKIP (black) to variants (red) indicates that RKIP adopts different conformational states upon S153 phosphorylation or mutation of residues involved in the salt bridge, whereas the phosphomimetic $RKIP^{S153E}$ is insufficient to induce the change. Peaks corresponding to S153 and E135 and the random coil region (dashed circle in *A*, *C*, and *D*) are highlighted. In the variants, the E135 peak is unperturbed only in S153E. Spectra were obtained at 25 °C. (*G*) Location of residues perturbed in the HSQC spectra of $RKIP^{K157A}$ (magenta) and $RKIP^{D134A,E135A}$ (magenta and blue).

enhanced stability enabled the pS153-K157 salt bridge to outcompete the D134/E135-K157 salt bridge and initiate the events leading to partial unfolding of the loop. Since typical single (+,−) salt bridges are generally weak (15), this result also provided a rationale for why some S-to-E phosphomimetics do not function as well as the phosphorylated versions.

In our "salt-bridge theft" model, the breakage of the D134/E135-K157 salt bridge is the critical event. To test the model, we disrupted the triad with an additional K157E substitution. As anticipated, this RKIP^{S153E,K157E} variant had an HSQC spectrum matching that of RKIP^{pS153} (Fig. 2 *C* and *D* and *SI Appendix*, Fig. S2). Furthermore, few spectral differences were observed between the single RKIP^{K157E} and the double RKIP^{S153E,K157E} variants, indicating that the single K157E substitution was sufficient to trigger the conformational switch. We also examined less disruptive alanine substitutions on either the helix or the loop side, K157A and D134A/E135A, respectively. These substitutions caused structural changes approaching those seen in RKIP^{K157E}, consistent with the loss of the salt bridge (Fig. 2 *E* and *F* and *SI Appendix*, Fig. S2). Substitution with larger tyrosine residues (D134Y/E135Y) also resulted in perturbations similar to those seen in K157E (*SI Appendix*, Fig. S2).

To clarify the nature of the differences between the K157 mutants substituted with charged versus uncharged residues, we analyzed an overlay of the K157E and K157A NMR spectra (*SI Appendix*, Fig. S2). This overlay highlights the differences observed between K157E and K157A, which are especially notable in the random coil region in the NMR spectrum of K157E and indicative of increased unfolding (Fig. 2*D*). This difference likely was a reflection of the more disruptive effects of three colocalized carboxylic acids in K157E versus two colocalized carboxylic acids in K157A.

Salt-bridge disruption in RKIP^{K157A} caused a near-complete or total loss of NMR peak intensity for various residues including L68, L103, S104, V107, G108, E135, L138, R146, G147, and L184 (peaks for the intervening residues E105-Y106 and P136-N145 could not be resolved) (Fig. 2*G*). The perturbed residues in the RKIP^{D134A,E135A} HSQC spectrum overlapped with those seen for RKIP^{K157A} but also included N132 and C133 (Fig. 2*G*). Some peaks in the mutants were selectively lost while others had native-like intensities, suggesting that the region from L103 to G147 is partially unfolded upon disruption of the native salt-bridge triad.

The disruption of the D134/E135 loop upon the theft of K157 likely resulted from an electrostatic repulsion of the adjacent D134 and E135 residues. Studies of the pK shifts for a pair of neighboring glutamic acids by McIntosh and coworkers (16) noted a pK_a increase for a glutamic acid of two units. This shift translates into an ∼3 kcal·mol^{-1} increase in proton affinity to the carboxylic acid, presumably resulting from the heightened negative potential due to the presence of the second glutamic acid. To create the heightened negative potential, additional energy is required to fold the protein with two nearby glutamic acids. There are also several other examples of single ionic locks that trigger dramatic structural reorganizations within a protein to facilitate protein activity-state transitions. For example, a similar E/DRY motif can be found in GPCRs with salt-bridge interactions between R and both E and D residues in consecutive positions (17). This salt bridge creates an ionic lock, maintaining the receptors in an inactive state. Mutagenesis of R is sufficient to transition the receptor to an active state. This motif is on the cytosolic face of the GPCR and therefore is not shielded from the influence of polar solvent or ionic interactions. Together, these studies suggest that RKIP has evolved to use the repulsion of two nearby glutamic acids to drive partial unfolding of a loop region.

Analysis of GRK2 binding provided further evidence for the functional role of residues within the salt-bridge triad. To determine the degree to which RKIP^{K157E} is a surrogate for RKIP^{pS153}, we compared the ability of RKIP^{K157E} to bind GRK2 with that of RKIP^{pS153} and the double variant RKIP^{S153E,K157E} in 293T cells by coimmunoprecipitation (14). For all cell studies, we mutated S153 to either an alanine or a glutamic acid to prevent S153 phosphorylation. As previously observed (14), the RKIP^{S153E,K157E} variant bound GRK2 instead of Raf-1 (Fig. 3). No significant difference in GRK2 binding was noted between RKIP^{pS153}, generated by treating cells with phorbol-12-myristate-13-acetate (PMA), and the two variants RKIP^{S153A,K157E} and RKIP^{S153E,K157E} (Fig. 3 *A* and *C*). The triple alanine variant RKIP^{S153A,D134A,E135A} was similarly able to bind to GRK2 (Fig. 3 *B* and *D*). By contrast, GRK2 binding to the double-alanine variant RKIP^{S153A,K157A} was not statistically significant, possibly reflecting the more limited structural perturbation noted above. These findings provide additional support for both the disruption of the salt-bridge triad and the partial unfolding of the associated region as critical events leading to the GRK2-binding–competent state.

The crystal structure of an RKIP variant lacking residues 143–146 further validated our model. R146 is highly conserved, and this region is altered by the P74L mutation that increases S153 phosphorylation (10). The initial motivation for designing this deletion mutant was to mimic the conformational changes induced by S153 phosphorylation to further dissect the molecular mechanism of the Raf1-to-GRK2 switch of RKIP. The RKIP$^{Δ143–146}$ deletion variant does indeed mimic the phosphorylated RKIP^{pS153} state (14). RKIP$^{Δ143–146}$ binds GRK2 to a comparable level as RKIP^{pS153} and similarly to RKIP^{pS153}, binds poorly to Raf1 (14). In addition, the deletion variant does not require S153 phosphorylation for these effects (14), further demonstrating that Δ143–146 largely simulates the structural change in RKIP^{pS153} induced by phosphorylation. We solved the crystal structure of RKIP$^{Δ143–146}$ at a moderate resolution (2.7 Å) (Fig. 4 *B* and *C* and *SI Appendix*, Table S1). Notably, E135 now points away from K157 and no longer participates in the salt bridge (Fig. 4 *D* and *E*), leaving a salt

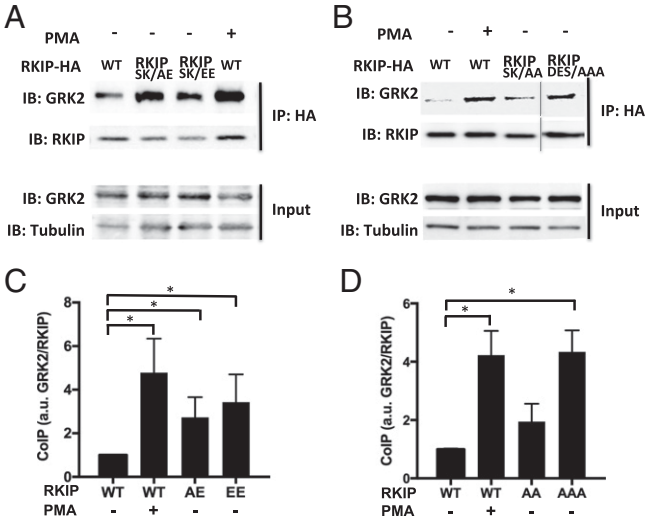

Fig. 3. In vivo interactions between GRK2 and salt-bridge mutants of RKIP. (*A* and *B*) Cells expressing WT HA-RKIP or HA-RKIP variants were incubated with or without PMA (1 μM) for 10 min before precipitation with an anti-HA antibody and blotted for GRK2. Input represents 10% of total lysates used for immunoprecipitation assays: Representative coimmunoprecipitation assays using RKIP mutants (*A*) S153A/K157E (SK/AE) or S153E/K157E (SK/EE) or (*B*) S153A/K157A (SK/AA) or D134A/E135A/S153A (DES/AAA) are shown. (*C* and *D*) Plots of GRK2 bound to RKIP mutants: S153A/K157E (AE); S153E/K157E (EE); S153A/K157A (AA); D134A/E135A/S153A (AAA). Average of blot densities for GRK2 normalized to RKIP using (*C*) four or (*D*) three independent experiments including *A* is shown. Error bars indicate SEM. *$P < 0.05$ by a one-tailed Student's *t* test.

bridge only between D134 and K157. Evidently, this interaction is too weak to maintain the original Raf-binding structure in solution (14). In addition, regions near R146 seem to be more flexible compared with other regions of the crystal structure indicated by larger B-factors relative to the average B-factor of the entire structure, suggesting that this part of the protein is perturbed. The RKIP$^{\Delta 143–146}$ variant therefore serves as a useful tool to underscore the importance of local perturbation and partial unfolding of RKIP for GRK2 binding.

Since oligomerization could alter the interpretation of the NMR data, we examined whether RKIP forms a dimer by size-exclusion chromatography, multi-angle light scattering, and SDS/PAGE (*SI Appendix*, Figs. S3 and S4). Reduced RKIP^{K157E} and RKIP^{S153E,K157E} were nearly identical in size and molecular weight to monomeric WT RKIP (*SI Appendix*, Fig. S4). Furthermore, RKIP$^{\Delta 143–146}$ crystallized as a monomer. Whereas RKIP may form oligomers in cells (14), phosphorylation at S153 transitions RKIP between monomeric states under reducing conditions.

The salt-bridge theft mechanism in RKIP involves breaking a salt bridge, which subsequently enables a switch in protein partners. We reasoned that a similar disruption of a salt bridge formed across a binding interface could be widespread in complexes controlled by phosphorylation. Consequently, we performed a bioinformatic search on ∼5,000 hetero-oligomers taken from a curated data set (18) to look for key features involving a phosphorylatable S/T *pSite*, a K or R *Switch*(+) and at least one D or E salt-bridge *Partner*(−) (Fig. 1*B*). The salt-bridge theft motif is defined as follows: (*i*) the *pSite* and *Switch*(+) are on the same chain at least two residues apart, while the *Partner*(−) is on another chain; (*ii*) the *Switch*(+) and *Partner*(−) are in contact with side chains within 3 Å (19); (*iii*) the Cα atoms of the *pSite* and the *Switch*(+) are within 8 Å (20, 21); (*iv*) the *pSite* is on the surface with a relative solvent accessible area above 25% (22, 23); (*v*) the *pSite* is a known or predicted phosphorylation site (24, 25); and (*vi*) the *pSite* is not at the binding interface, having no heavy atoms within 3 Å from any interfacial residue (19).

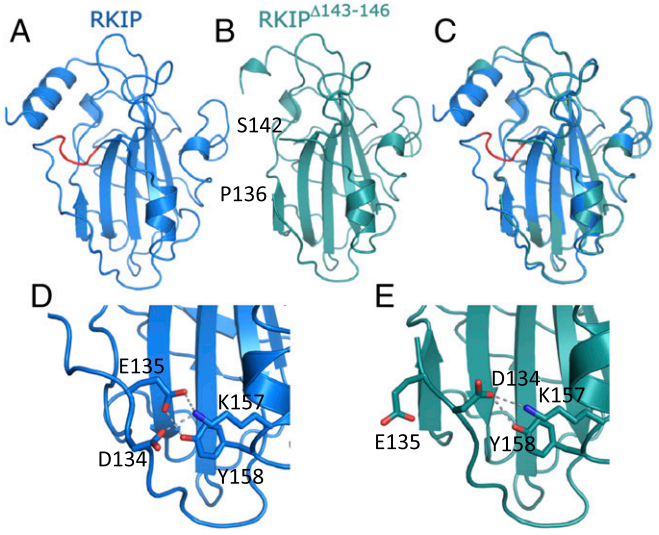

Fig. 4. Crystal structures of WT RKIP (6ENS) and the RKIP deletion mutant (6ENT). (*A*) Ribbon presentation of the WT structure of RKIP. Highlighted in red are the residues deleted in the RKIP$^{\Delta 143–146}$ variant. (*B*) Ribbon presentation of the RKIP$^{\Delta 143–146}$ variant. The location of the residues flanking the deletion are noted. (*C*) Superposition of WT RKIP (blue) and the RKIP$^{\Delta 143–146}$ variant (green). (*D*) Interactions of residue E135 with K157 and D134 in WT RKIP. Dashed lines indicate salt bridges and hydrogen bonds. (*E*) Interactions of residue D134 with K157 and Y158 in the RKIP$^{\Delta 143–146}$ variant.

This analysis identified 33% (1,602/4,857) of total hetero-oligomers as having the necessary criteria for the salt-bridge theft mechanism with either known (5%) or predicted (28%) phosphorylation sites (Fig. 5*A* and *SI Appendix*, Tables S2 and S3). A similar analysis of homo-oligomers (18) revealed a 10% occurrence of the salt-bridge theft motif (2,048/20,685). From this set, along with additional criteria found in RKIP (namely, i and i+4 are in a helix and have two D/E in contact with K/R), we identified three candidates that had been previously studied by mutation or phosphorylation: Bax (1F16.pdb), Troponin I and C (1J1D, chains A and C), and Early Endosome Antigen 1 (EEA1) (1JOC, chains A and B). In RKIP, Bax, and Troponin I, the S/T-K pair was located at positions i and i+4 on an α-helix, whereas in EEA1, the i, i+4 pair was present in a β-turn.

We postulate that the salt-bridge theft mechanism in Bax regulates local conformational changes along a single polypeptide chain that eventually leads to Bax oligomerization (26). Bax, an apoptotic protein that triggers release of cytochrome *c* from mitochondria (27), forms a salt bridge between K64 and D33 on two adjacent helices in its inactive "closed" conformation (Fig. 5*B*) (28). We expect that phosphorylation of S60 should appropriate K64, triggering the separation of the two helices to generate the active "open" conformation. This event facilitates oligomerization leading to cytochrome *c* release. In support of the theft mechanism, the loss of the interhelical salt bridge upon either a K64D or D33A mutation triggers cytochrome *c* release whereas the S60A mutation, which prevents phosphorylation, inhibits cytochrome *c* release (29). As in RKIP, a phosphomimetic substitution of the serine residue (S60D) was insufficient to fully activate Bax or trigger cytochrome *c* release, presumably because the singly charged residue, unlike the authentic phosphorylated serine, cannot outcompete the K64-D33 salt bridge (29).

The phosphorylation of Troponin I regulates heterodimer formation with Troponin C. Troponin C is a calcium-binding protein that interacts with Troponin I, eliciting a conformational change in Troponin I and muscle contraction (30). Phosphorylation of Troponin I at S42 on an α-helix in chain C disrupts the Troponin C/I interaction, releasing myofilament tension and decreasing sliding speed (31). K46 on Troponin I likely forms a salt bridge with D2 and D139 on Troponin C that is lost upon phosphorylation of S42 (Fig. 5*B*). Consistent with the theft mechanism, combining S42E and S44E substitutions decreases fiber tension and calcium sensitivity, whereas the S42A mutation enhances both parameters (32).

The phosphorylation of the homodimer EEA1 controls binding to phospholipids (33, 34), mediating endosomal trafficking by binding to phospholipid vesicles via phosphatidylinositol-3-phosphate (35). Phospholipid binding requires phosphorylation of T1392, and its mutation to alanine (T1392A) decreases this interaction (36, 37). The T1392 phosphorylation should attract K1396 (both on chain B), triggering a salt-bridge theft and freeing the salt-bridge partners (the adjacent D1352 and E1351 on chain A) to undergo local rearrangement and generate a new homodimer interface that interacts with endosomes (Fig. 5*B*) (33, 34).

The high frequency of the salt-bridge theft motif in hetero-oligomers suggests that it occurred early in evolution. Consistently, our motif search revealed a higher prevalence among invertebrates (38 ± 1%) relative to vertebrates (28 ± 1%) (Fig. 5*A* and *SI Appendix*, Table S2). However, RKIP (PEBP1) acquired S153 later in evolution whereas E135 and K157 are two of the most conserved residues within the PEBP family (*SI Appendix*, Fig. S5 and Table S4), indicating that this salt bridge antedates acquisition of the salt-bridge theft mechanism. Bax, EEA1, and Troponin I similarly acquired the salt-bridge theft motif at the vertebrate stage (*SI Appendix*, Fig. S5 and Tables S5–S7). Thus, the salt-bridge theft motif as a mediator of protein interactions is poised for regulation by the nascent kinome but

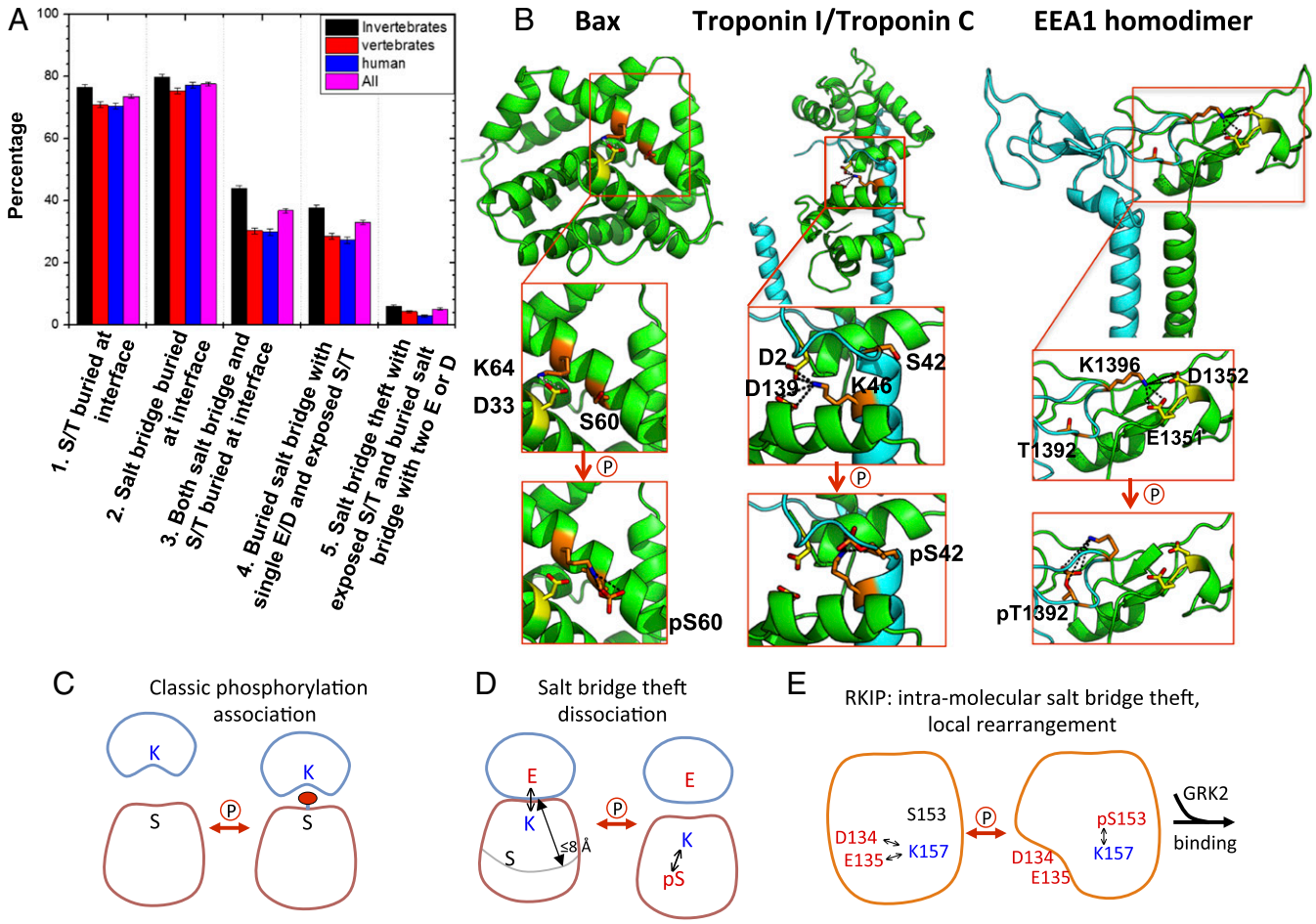

Fig. 5. Salt-bridge theft mechanism observed in RKIP and other proteins. (*A*) Bar plot of the frequencies of different interfacial properties among hetero-oligomers on a per-complex basis. Errors are the SD calculated assuming a binomial distribution. See *SI Appendix*, Table S2, for details. (*B*) Phosphorylation of Bax at S60 by PKA attracts K64, destabilizing the α-helix and activating translocation and cytochrome *c* release. Residues involved in the salt bridge (K64, D33) are indicated. Phosphorylation at S42 by PKC prevents the interaction of Troponin I (blue) with Troponin C (green) and inhibits Troponin I activity. Residues involved in the salt bridge are indicated (K46 on chain C; D2 and D139 on chain A). Phosphorylation of EEA1 at T1392 on chain B by the kinase p38 attracts K1396 on chain B, thus freeing D1352 on chain A to interact with phosphatidylinositol-3-phosphate within the endosomal membrane. Residues involved in the salt bridge are indicated (K1396 on chain B; D1352 and possibly E1351 on chain A). (*C*–*E*) Alternative models for phosphorylation-controlled protein association.

may also be acquired later in evolution along with an expanded role for the kinome.

The salt-bridge theft mechanism that we describe here differs from the classic view of phosphorylation-controlled binding through protein domains, as exemplified by SH2 and 14–3-3 domains (38). In the latter case, the phosphorylation of a serine or threonine situated at the interface promotes binding (Fig. 5*C*). This mechanism involves an initially solvent-exposed serine or threonine. Possibly, the phosphorylation of residues at the interface could lead to dissociation; in this situation, however, the residues would not be as solvent-accessible. The high frequency (73%) of a hetero-oligomeric protein interface having either a serine or a threonine suggests that this is a viable mechanism for regulating oligomeric protein interactions (Fig. 5*A* and *SI Appendix*, Table S3), as supported by recent studies (3).

In contrast, our salt-bridge theft mechanism involves solvent-exposed serine or threonine residues that are not directly on the binding interface (Fig. 5 *D* and *E*). The mechanism builds on the high frequency of salt bridges (77%) at hetero-oligomeric protein interfaces (Fig. 5*A* and *SI Appendix*, Table S3). These charged residues are enriched two- to threefold at binding interfaces, as noted previously (39). By contrast, the frequency of S/T residues is the same throughout the protein whether on or near the interface or buried within the protein (*SI Appendix*, Table S3). If a solvent-exposed S/T is close enough to an interfacial salt bridge, then a pSer/pThr can compete for the bridge. Because only ∼30% of the protein interfaces feature the salt-bridge theft motif whereas salt bridges are present 77% of the time, the availability of S/T residues near the interface appears to be a limiting condition. When two acidic residues participate in the salt bridge, more extensive conformational changes can occur. This option is present at lower levels than the salt-bridge dyads for both hetero-oligomers (5%) and homo-oligomers (1%) (*SI Appendix*, Table S2).

Whereas the traditional model posits that phosphorylation modulates protein interactions by directly altering the binding interface, the salt-bridge theft mechanism has several advantages as an additional route for regulation by the kinome. Due to solvent accessibility, the theft allows for facile removal or addition of the phosphate whereas direct binding across the interface allows only for facile phosphorylation. Therefore, phosphorylation leading to interface disruption would be more likely to occur with the salt-bridge theft mechanism. In support of this hypothesis, the examples that we have highlighted here for the salt-bridge theft all

involve phosphorylation-induced disruption of protein interactions. Troponin I phosphorylation dissociates a heterodimer, and EEA1 disrupts a homodimer (Fig. 5*D*), whereas RKIP and Bax phosphorylation disrupt interacting polypeptide chains within a single protein, enabling local unfolding that facilitates binding to GRK2 (Fig. 5*E*) or Bax, respectively.

Finally, disruption of the salt bridge, especially one that involved two negative charges, may induce protein remodeling through partial unfolding due to the colocalization of two negatively charged side chains. Similar reorganizations of electrostatic networks and allosteric effects resulting from disrupted charge clusters have also been observed in other systems, including PKA and VraR (40, 41). These examples as well as others (42) suggest that neither mono- nor divalent cation binding would completely recover the energy invested in the colocalization of D134 and E135 in RKIP, and, thermodynamically, the partial unfolding of the loop is favored.

In this article, we have demonstrated the presence of a phosphorylation-triggered salt-bridge competition or "theft" mechanism for regulating RKIP/GRK2 association. The motif exists in one-third of hetero-oligomers and is enriched in invertebrates. The mechanism could be an early mode of introducing phosphorylation-controlled binding, in part as it uses an existing salt bridge, an interaction known to be enhanced at protein–protein interfaces (39). The original salt bridge is left intact, in contrast to serine phosphorylation that directly participates in the salt bridge across an interface (43). Thus, the regulation using the theft mechanism is controlled through a nearby solvent-accessible residue that would be easier to substitute or phosphorylate. Our computational analysis suggests that this mechanism may be broadly operative in controlling protein oligomerization.

Materials and Methods

NMR Experiments. All HSQC spectra were collected on a 500-MHz magnet with a Bruker AVANCE III console at 25 °C with a typical protein concentration of 0.5 mM. Spectra were processed using NMR Pipe and CARA software packages.

Phosphorylation for NMR Studies. A 400 μM ^{15}N RKIP^{P74L} solution was prepared in 20 mM Hepes, pH 7.5, with 0.5 mM EGTA, 2 mM DTT, and 200 nM PKC. $MgCl_2$ and ATP were then added to final concentrations of 5 mM each. Phosphorylation was carried out at 37 °C for 10 h before being reduced to 25 °C for NMR measurements.

Further descriptions of the methods are listed in *SI Appendix, SI Materials and Methods*.

ACKNOWLEDGMENTS. We thank Helmholtz-Zentrum Berlin for the allocation of synchrotron radiation beamtime and the staff of beamline MX 14.1 for technical assistance and Drs. Gianluigi Veglia and Jonggul Kim for valuable discussions. This work was supported by Grants GM087630 (to M.R.R.), GM55694 (to T.R.S.), Deutsche Forschungsgemeinschaft FZ82 (to K.L., C.K., and H.S.) and SFB688 and TPA17 (to K.L.), the German Ministry of Research and Education and the Ministry for Innovation, Science and Research of the Federal State of North Rhine-Westphalia (K.L.).

1. Hunter T (2012) Why nature chose phosphate to modify proteins. *Philos Trans R Soc Lond B Biol Sci* 367:2513–2516.
2. Davis FP (2011) Phosphorylation at the interface. *Structure* 19:1726–1727.
3. Nishi H, Hashimoto K, Panchenko AR (2011) Phosphorylation in protein-protein binding: Effect on stability and function. *Structure* 19:1807–1815.
4. Fu Z, et al. (2006) Metastasis suppressor gene Raf kinase inhibitor protein (RKIP) is a novel prognostic marker in prostate cancer. *Prostate* 66:248–256.
5. Dangi-Garimella S, et al. (2009) Raf kinase inhibitory protein suppresses a metastasis signalling cascade involving LIN28 and let-7. *EMBO J* 28:347–358.
6. Yun J, et al. (2011) Signalling pathway for RKIP and Let-7 regulates and predicts metastatic breast cancer. *EMBO J* 30:4500–4514.
7. Schmid E, et al. (2015) Cardiac RKIP induces a beneficial β-adrenoceptor-dependent positive inotropy. *Nat Med* 21:1298–1306.
8. Lorenz K, Rosner MR, Brand T, Schmitt JP (2017) Raf kinase inhibitor protein: Lessons of a better way for β-adrenergic receptor activation in the heart. *J Physiol* 595: 4073–4087.
9. Banfield MJ, Barker JJ, Perry AC, Brady RL (1998) Function from structure? The crystal structure of human phosphatidylethanolamine-binding protein suggests a role in membrane signal transduction. *Structure* 6:1245–1254.
10. Granovsky AE, et al. (2009) Raf kinase inhibitory protein function is regulated via a flexible pocket and novel phosphorylation-dependent mechanism. *Mol Cell Biol* 29: 1306–1320.
11. Clark MC, et al. (2006) NMR assignment of rat Raf kinase inhibitor protein. *J Biomol NMR* 36:4.
12. Corbit KC, et al. (2003) Activation of Raf-1 signaling by protein kinase C through a mechanism involving Raf kinase inhibitory protein. *J Biol Chem* 278:13061–13068.
13. Lorenz K, Lohse MJ, Quitterer U (2003) Protein kinase C switches the Raf kinase inhibitor from Raf-1 to GRK-2. *Nature* 426:574–579.
14. Deiss K, Kisker C, Lohse MJ, Lorenz K (2012) Raf kinase inhibitor protein (RKIP) dimer formation controls its target switch from Raf1 to G protein-coupled receptor kinase (GRK) 2. *J Biol Chem* 287:23407–23417.
15. Errington N, Doig AJ (2005) A phosphoserine-lysine salt bridge within an alpha-helical peptide, the strongest alpha-helix side-chain interaction measured to date. *Biochemistry* 44:7553–7558.
16. Platzer G, Okon M, McIntosh LP (2014) pH-dependent random coil (1)H, (13)C, and (15)N chemical shifts of the ionizable amino acids: A guide for protein pK a measurements. *J Biomol NMR* 60:109–129.
17. Rovati GE, et al. (2017) The DRY motif and the four corners of the cubic ternary complex model. *Cell Signal* 35:16–23.
18. Levy ED, Pereira-Leal JB, Chothia C, Teichmann SA (2006) 3D complex: A structural classification of protein complexes. *PLoS Comput Biol* 2:e155.
19. Xue LC, Dobbs D, Bonvin AM, Honavar V (2015) Computational prediction of protein interfaces: A review of data driven methods. *FEBS Lett* 589:3516–3526.
20. Wang S, Sun S, Li Z, Zhang R, Xu J (2017) Accurate de novo prediction of protein contact map by ultra-deep learning model. *PLoS Comput Biol* 13:e1005324.
21. Monastyrskyy B, D'Andrea D, Fidelis K, Tramontano A, Kryshtafovych A (2014) Evaluation of residue-residue contact prediction in CASP10. *Proteins* 82:138–153.
22. Ma J, Wang S (2015) AcconPred: Predicting solvent accessibility and contact number simultaneously by a multitask learning framework under the conditional neural fields model. *Biomed Res Int* 2015:678764.
23. Yan C, Wu F, Jernigan RL, Dobbs D, Honavar V (2008) Characterization of protein-protein interfaces. *Protein J* 27:59–70.
24. Xue Y, et al. (2005) GPS: A comprehensive www server for phosphorylation sites prediction. *Nucleic Acids Res* 33:W184–W187.
25. Ullah S, et al. (2016) dbPAF: An integrative database of protein phosphorylation in animals and fungi. *Sci Rep* 6:23534.
26. Sung TC, et al. (2015) Solution structure of apoptotic BAX oligomer: Oligomerization likely precedes nembrane insertion. *Structure* 23:1878–1888.
27. Zheng JH, Viacava Follis A, Kriwacki RW, Moldoveanu T (2016) Discoveries and controversies in BCL-2 protein-mediated apoptosis. *FEBS J* 283:2690–2700.
28. Cartron PF, et al. (2002) Involvement of the N-terminus of Bax in its intracellular localization and function. *FEBS Lett* 512:95–100.
29. Arokium H, et al. (2007) Substitutions of potentially phosphorylatable serine residues of Bax reveal how they may regulate its interaction with mitochondria. *J Biol Chem* 282:35104–35112.
30. Burkart EM, et al. (2003) Phosphorylation or glutamic acid substitution at protein kinase C sites on cardiac troponin I differentially depress myofilament tension and shortening velocity. *J Biol Chem* 278:11265–11272.
31. Kooij V, et al. (2013) PKCα-specific phosphorylation of the troponin complex in human myocardium: A functional and proteomics analysis. *PLoS One* 8:e74847.
32. Pyle WG, Sumandea MP, Solaro RJ, De Tombe PP (2002) Troponin I serines 43/45 and regulation of cardiac myofilament function. *Am J Physiol Heart Circ Physiol* 283: H1215–H1224.
33. Callaghan J, Simonsen A, Gaullier JM, Toh BH, Stenmark H (1999) The endosome fusion regulator early-endosomal autoantigen 1 (EEA1) is a dimer. *Biochem J* 338: 539–543.
34. Macé G, Miaczynska M, Zerial M, Nebreda AR (2005) Phosphorylation of EEA1 by p38 MAP kinase regulates mu opioid receptor endocytosis. *EMBO J* 24:3235–3246.
35. Dumas JJ, et al. (2001) Multivalent endosome targeting by homodimeric EEA1. *Mol Cell* 8:947–958.
36. Ramanathan HN, Zhang G, Ye Y (2013) Monoubiquitination of EEA1 regulates endosome fusion and trafficking. *Cell Biosci* 3:24.
37. Burd CG, Emr SD (1998) Phosphatidylinositol(3)-phosphate signaling mediated by specific binding to RING FYVE domains. *Mol Cell* 2:157–162.
38. Pawson T, Nash P (2003) Assembly of cell regulatory systems through protein interaction domains. *Science* 300:445–452.
39. Xu D, Tsai CJ, Nussinov R (1997) Hydrogen bonds and salt bridges across protein-protein interfaces. *Protein Eng* 10:999–1012.
40. P Barros E, et al. (2017) Electrostatic interactions as mediators in the allosteric activation of protein kinase a RIα. *Biochemistry* 56:1536–1545.
41. Leonard PG, Golemi-Kotra D, Stock AM (2013) Phosphorylation-dependent conformational changes and domain rearrangements in Staphylococcus aureus VraR activation. *Proc Natl Acad Sci USA* 110:8525–8530.
42. Draper DE (2004) A guide to ions and RNA structure. *RNA* 10:335–343.
43. Pearlman SM, Serber Z, Ferrell JE, Jr (2011) A mechanism for the evolution of phosphorylation sites. *Cell* 147:934–946.

Supplementary Material and Methods

Cell culture. HEK293T cells were maintained in DMEM high glucose supplemented with 10% fetal bovine serum (Gibco), penicillin (50 U/ml, Life Technology), and streptomycin (50 µg/ml, Life Technology). For stable cell lines, cells were transfected with lenti-viral shRNA to silence human endogenous RKIP, followed by puromycin selection (0.2 µg/ml) for one week. Then rat wild type RKIP or RKIP mutants were transiently transfected using the *Trans*IT-LT1 transfection reagent (Mirus) and OPTI-MEM (Gibco).

RKIP mutations. RKIP mutants (S153A/K157A, S153A/K157E, S153E/K157E, D134A/E135A/S153A) were generated using a QuikChange II site-directed mutagenesis kit (Agilent Technologies) with a wild type (WT) RKIP carrying a HA tag in the pCDNA3.1 vector. All of the RKIP mutants generated were sequence validated at the University of Chicago Comprehensive Cancer Center (cancer-seqbase.uchicago.edu).

Antibodies and Chemicals. GRK2 (sc-13143, Santa Cruz), RKIP (sc-5423, Santa Cruz), HA high affinity (Roche), alpha tubulin (sc-8035, Santa Cruz) and Normal IgG (sc-2027, Santa Cruz) were used for *in vivo* protein analyses. Phorbol 12-myristate 13-acetate (PMA) was purchased from Sigma.

Co-immunoprecipitation (CoIP) assays. HEK293T-shRKIP cells ($1X10^6$) were transiently transfected for exogenous expression of wild type (WT) and mutant rat RKIP-HA tag along with a GRK2 expressing plasmid (2 µg). Transfected cells were followed by serum starvation overnight and treated for PMA (0.1 µM) for 10 min before collection of lysates in IP buffers (50 mM Tris pH 7.5, 150 mM NaCl, 0.25% Na-deoxycholate, 1% NP40, 1 mM EDTA) containing a protease inhibitor cocktail (Millipore) and phosphatase inhibitors (Goldbiosystem). Sonicated cell lysates were centrifuged at 11,000 *g* for 30 minutes at 4 °C and incubated with 25% protein G-sepharose 4 fast flow (GE Healthcare) with rabbit IgG for 1 hour at 4 °C to block non-specific binding with 25% G-sepharose. Precleared supernatants were precipitated using anti-HA antibody overnight at 4 °C followed by incubation with 25% G-

sheparose. Anti-HA immunoprecipitated proteins were assayed for GRK2 blotting on nitrocellulose membrane (Amersham Hybond ECL). Bands in the western blots were detected and quantified using Li-Cor Image studio.

Protein purification for crystallization. cDNAs coding for N-terminal His_6-tagged WT mouse RKIP (His-RKIP) and the rat RKIP variant (His-RKIP$^{\Delta 143\text{-}146}$) were cloned into the expression vector pET3c (Novagen). His-RKIP and the RKIP variants were expressed in *Escherichia coli* BL21(DE3)pLysS cells. For purification of His-RKIP and the His-RKIP$^{\Delta 143\text{-}146}$ variant the bacteria were thawed, resuspended and lysed in 50 mM Tris pH 7.4, 500 mM NaCl and 20 mM imidazole. The soluble fraction of the cell lysate was loaded onto a Ni Sepharose affinity column (Histrap, GE Healthcare/ ÄKTA), and eluted with a gradient to 500 mM imidazole (20 column volumes). The proteins were further purified by SEC (Superdex 200 26/60, GE Healthcare/ ÄKTA) in 20 mM PIPES pH 6.5, 150 mM NaCl and 1 mM EDTA. The protein samples were concentrated to up to 40 mg/ml, flash-frozen in liquid nitrogen and stored at −80°C.

Crystallization, Data collection and Structure Determination. 1 µl of WT RKIP at a concentration of 11 mg/ml in ddH_2O was mixed with 1 µl of the reservoir solution containing 25% PEG 6000 and 100 mM NaAcetate pH 4.6. The mixture was equilibrated in hanging drop vapor diffusion experiments at 20 °C against 1 ml of the reservoir solution. Crystals were flash frozen in liquid nitrogen utilizing mother liquor supplemented with 20% glycerol and data collection was performed at 100 K. The WT RKIP dataset was collected at beamline MX 14.1 (Bessy, Berlin).

His-RKIP$^{\Delta 143\text{-}146}$ was crystallized at a protein concentration of 15 mg/ml in a buffer containing 150 mM NaCl and 100 mM NaAcetate. 1 µl of the protein solution was mixed with 1 µl of the reservoir and the mixture was equilibrated in hanging drop vapor diffusion experiments at 20 °C against 1 ml of the reservoir solution, containing 17.5% PEG3350 and 100 mM NaF. Crystals were flash frozen in liquid nitrogen utilizing mother liquor supplemented with 20% glycerol and data collection was

performed at 100 K, and processed with iMOSFLM (44, 45). The dataset of the His-RKIP$^{\Delta 143\text{-}146}$ variant was collected at beamline MX 14.1 (Bessy, Berlin).

The structure of the WT protein was solved by molecular replacement using the program Phaser (46) and the structure of rat RKIP as a search model (pdb entry 2IQY). WT RKIP was refined with REFMAC5 (47, 48) and adjusted with Coot (49) incorporating anisotropic B-factor refinement. The structure of the His-RKIP $^{\Delta 143\text{-}146}$ variant was solved by molecular replacement with MOLREP (50) using the WT protein as search model and was refined with REFMAC5 (47). Structures of RKIP (6ENS) and the Δ143-146 variant (6ENT) were deposited in the Protein Data Bank.

Multi-angle light scattering (MALS). Studies of the oligomeric state used MALS coupled with SEC and were conducted with a Wyatt DAWN Heleos II Static Light Scattering unit and a WTC-05S5 column (100 Å pore size, 100-100,000 MW range) at room temperature.

Methods for the algorithms and analyses.

Blast algorithm:

All multiple sequence alignments (MSA) are extracted from UniProt BLAST(51, 52):

http://www.uniprot.org/blast/ with parameters as follows:

target DB	E-value	Matrix	Filtering	Gapped	TopHits
UniProtKB	0.001	BLOS-62	Filter_Low	Gap_Yes	1000_Hits

Select TopHits:

We extract top 500 sequences according to the ranking order of the Bit Scores (or, E-values). It should be noted that a high Bit Score or low E-value would indicate high sequence identity to the query sequence.

Multiple Sequence Alignment

We run Mafft (53) for these top 500 sequences to generate the final multiple sequence

alignment (MSA).

http://www.ebi.ac.uk/Tools/msa/mafft/

Statistics

The errors listed for Supplementary Tables 2 and 3, and Figure 4A are the standard deviations calculated assuming a binomial distribution.

Supplementary Figures S1-S5 and Tables S1-S7

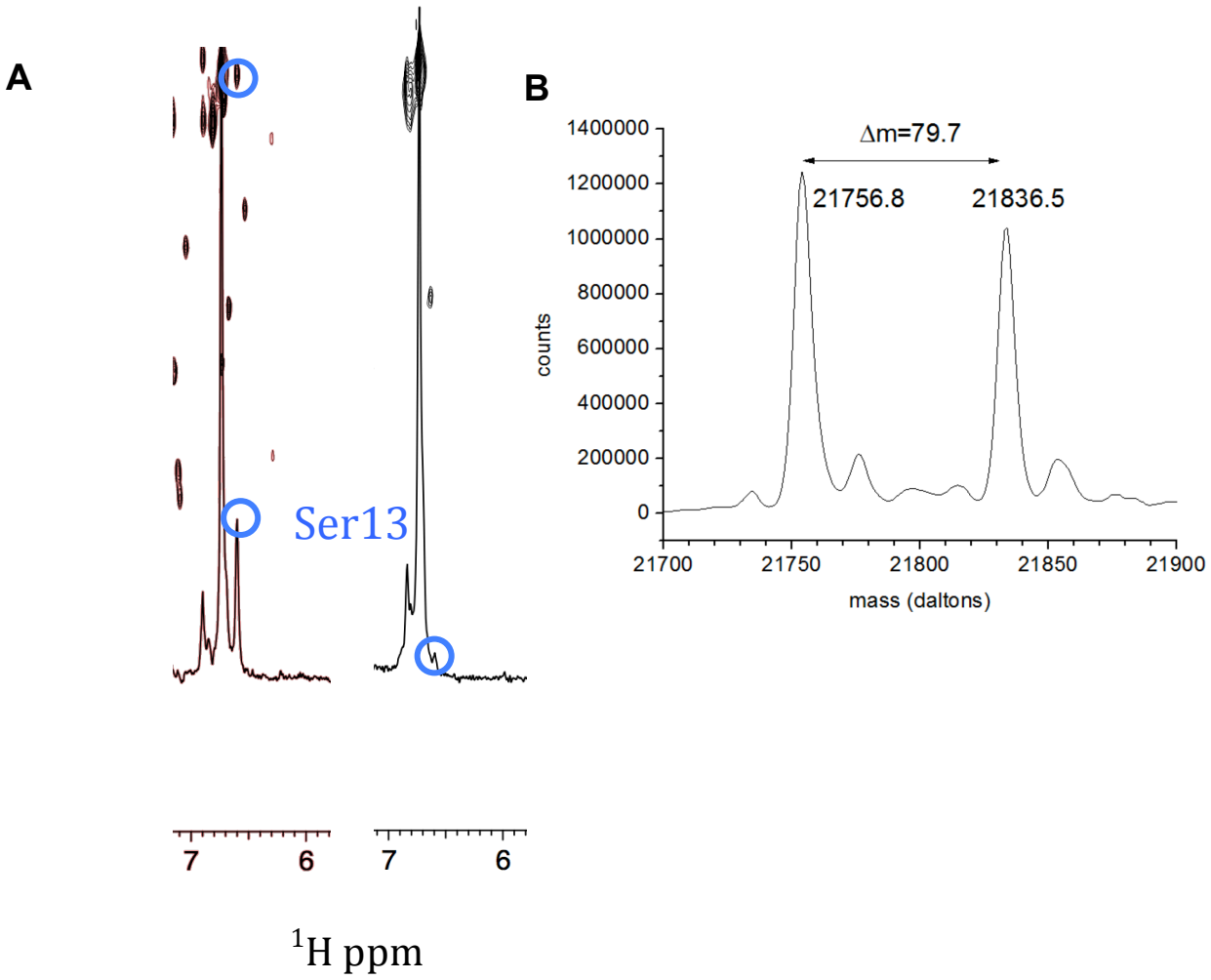

Supplementary Figure S1. Phosphorylation of S153. (A) Decrease in S153 NMR peak height due to phosphorylation (overlaid on the HSQC) **(B)** Mass spectrum of RKIP during phosphorylation process showing appropriate mass change (theoretical 80.0 daltons).

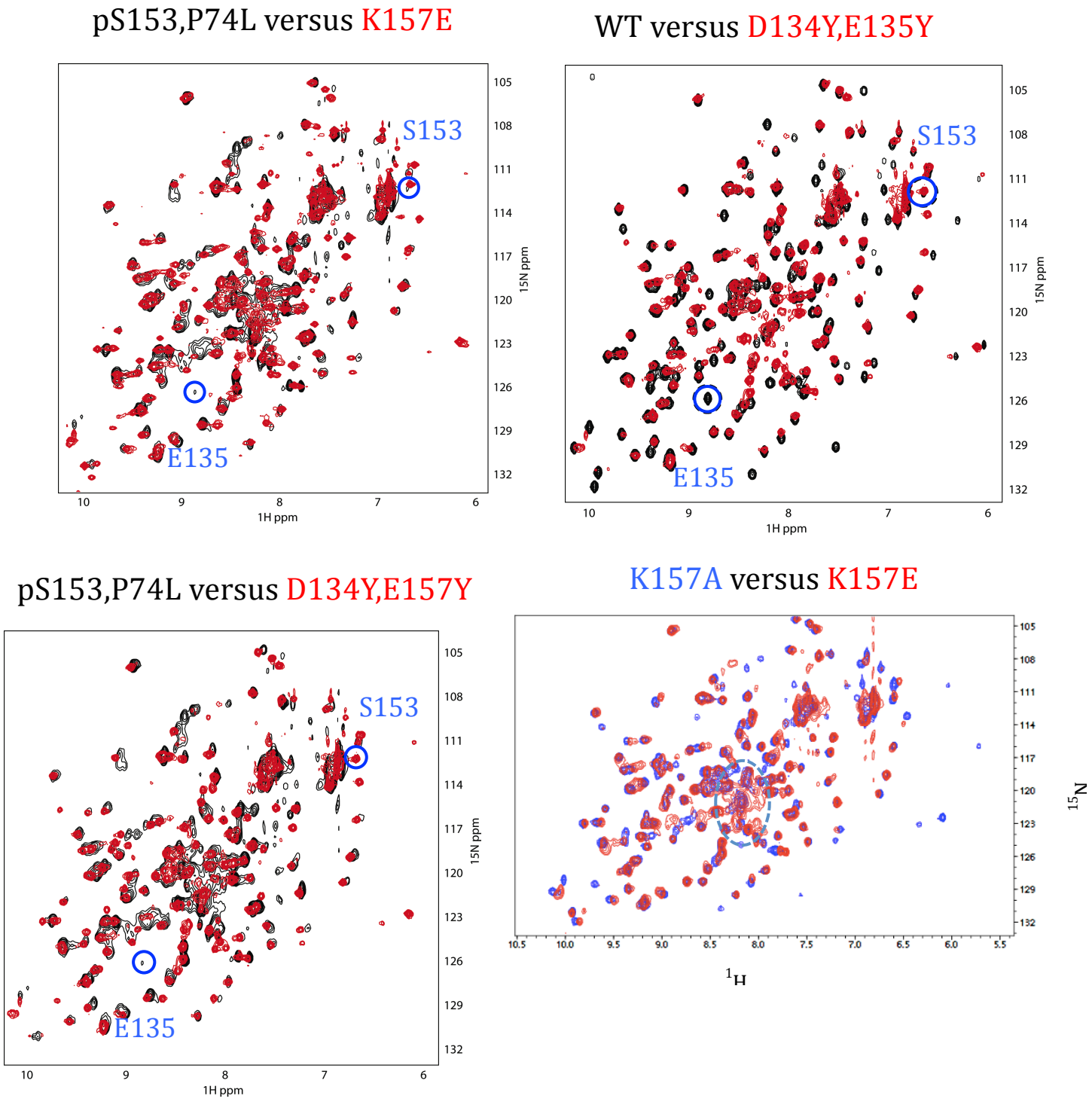

Supplementary Figure S2. Comparison of ^{15}N-^{1}H HSQC spectra at 25°C. The random coil region is highlighted (blue dashed circle).

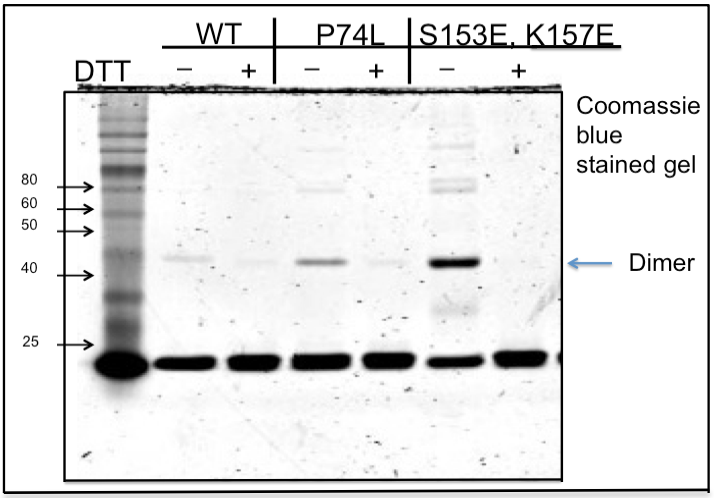

Supplementary Figure S3. Formation of RKIP oligomers is sensitive to reducing agents. Lysates from cells transfected with WT, P74L or S153E, K157E RKIP variants were boiled in the presence or absence of DTT. Samples were resolved by SDS PAGE and stained with Coomassie blue.

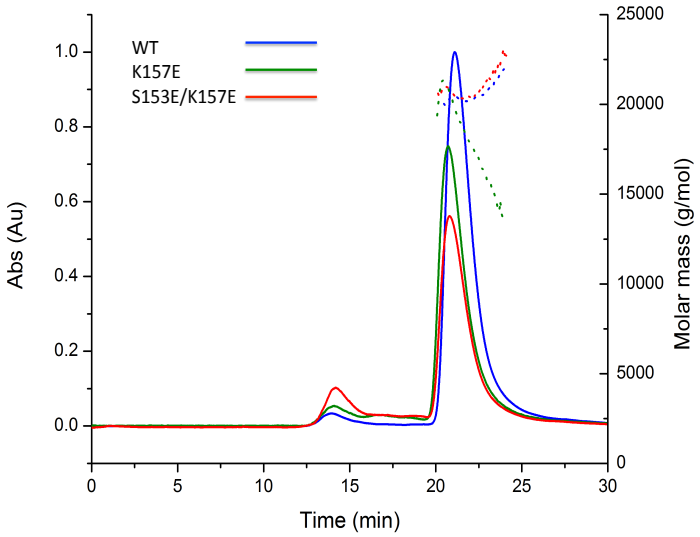

Supplementary Figure S4. Multi-angle light scattering (MALS) data indicating that RKIP is monomeric under reducing conditions. The small, high molecular weight peak observed by scattering did not exhibit UV absorbance (dotted line), suggesting that it is not proteinaceous.

a) RKIP (S153 and K157)

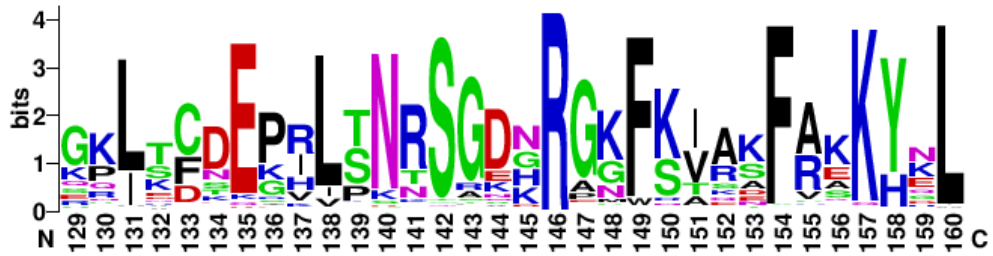

b) Bax (S60 and K64)

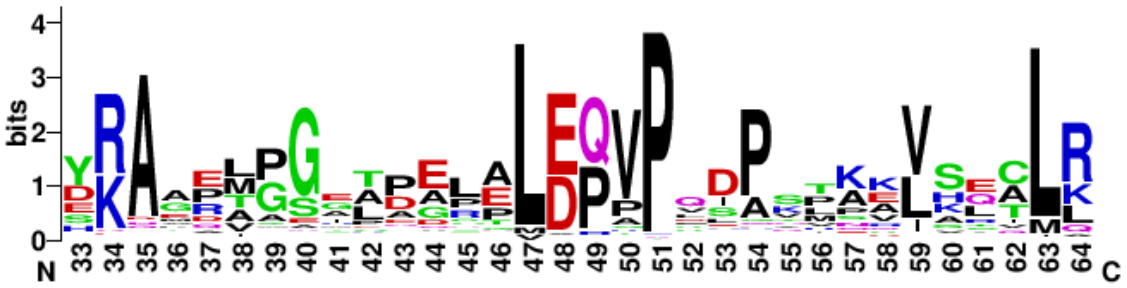

c) EEA1 (T1392 and K1396)

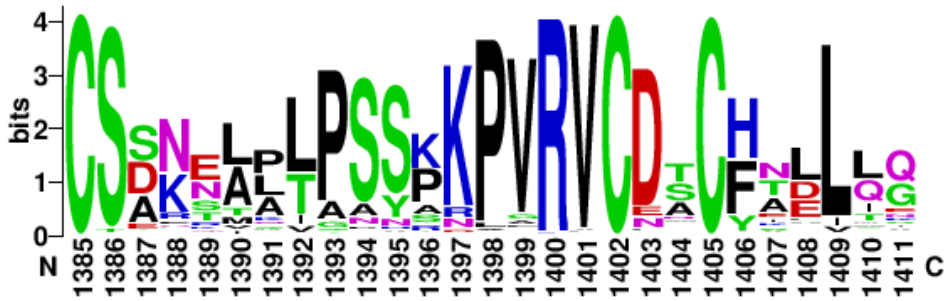

d) Troponin I (S42 and K46)

Supplementary Figure S5. Conserved Residues in Proteins with a Phosphotheft Motif. (a) Conserved residues within the RKIP (PEBP) family. (b) Conserved residues within the Bax family. (c) Conserved residues within the EEA1 family. (d) Conserved residues within the Troponin I family.

Table S1. Data collection and refinement statistics for RKIP wt and the His-RKIP$^{\Delta 143\text{-}6}$ variant.

Data collection	**Wild-type RKIP**	**RKIP$^{\Delta 143\text{-}6}$**
Wavelength	0.91841	0.91841
Space group	$P2_12_12_1$	I23
Unit cell parameters a/b/c (Å)	32.58 / 54.09 / 97.95	111.25/ 111.25/ 111.25
Resolution (Å)	23.06 - 1.3	55.63 – 2.66
Total reflections	172197	81287
Unique reflections	42630 (6048)	6706 (965)
Completeness (%)	98.5 (97.3)	100 (100)
Redundancy	4.0 (4.0)	12.1 (11.5)
R_{merge} (%)	8.2 (64.4)	10.6 (146.5)
R_{pim} (%)	4.6 (36.6)	3.2 (45.0)
$\langle I/\sigma(I)\rangle$	8.6 (2.0)	14.7 (1.8)
Refinement		
Total number of atoms	1717	1404
Protein	1451	1396
Water molecules	250	6
Glycerol	2	-
Acetate	1	-
Zn	-	1
Cl	-	1
R_{cryst} (%)^2	12.48	20.96
R_{free} (%)^2	16.81	25.04
r.m.s.d. from ideal values in		
Bond lengths (Å)^2	0.011	0.009
Bond angles (°)	1.559	1.322
Planar groups (Å)	0.008	0.005
Chiral centers (Å^3)	0.106	0.078
Coordinate error (Å)	0.035	0.293
Average B-values (Å^2)		
Protein	15.60	87.14
Water	27.54	70.71
Glycerin	28.57	-
Acetate	16.42	-
Zn	-	59.82
Cl	-	68.24
Ramachandran plot (favored/allowed/disallowed)	98.55/0.72/0.72	96.34/2.44/1.22
PDB code	5M0F	5M0G

Table S2.

Analysis of Phosphotheft Motif Among Hetero-oligomers on a per complex basis[1]

Parameter[1]	Invertebrates	Vertebrates	Human	All
S/T at interface	1790/2344=76.4 ± 0.88	1779/2513=70.8 ± 0.91	1426/2025=70.4 ± 1.01	3569/4857=73.5 ± 0.63
(Complex)	1068/1419=75.2 ± 1.14	1189/1633=72.8 ± 1.10	980/1376=71.2 ± 1.22	2257/3052=74.0 ± 0.79
Salt bridge at interface	1869/2344=79.7 ± 0.83	1893/2513=75.3 ± 0.86	1561/2025=77.1 ± 0.93	3762/4857=77.5 ± 0.60
(Complex)	1137/1419=80.1 ± 1.06	1277/1633=78.2 ± 1.02	1076/1376=78.2 ± 1.11	2414/3052=79.1 ± 0.74
Both S/T and Salt bridge at interface	1026/2344=43.8 ± 1.02	762/2513=30.3 ± 0.92	606/2025=29.9 ± 1.02	1788/4857=36.8 ± 0.69
(Complex)	637/1419=44.9 ± 1.32	533/1633=32.6 ± 1.16	423/1376=30.7 ± 1.24	1170/3052=38.3 ± 0.88
Phospho-theft Mechanism with one D/E	882/2344=37.6 ±1.00	720/2514=28.6 ± 0.90	553/2025=27.3 ± 0.99	1602/4857=32.9 ± 0.67
(Complex)	533/1419=37.6 ± 1.28	490/1636=30.0 ± 1.13	389/1376=28.3 ± 1.21	1023/3052=33.5 ± 0.85
Phospho-theft Mechanism with two D/E's	144/2344=6.1 ± 0.50	107/2513=4.3 ± 0.40	58/2025=2.9 ± 0.37	251/4857=5.2 ± 0.32
(Complex)	95/1419=6.7 ± 0.66	80/1633=4.9 ± 0.53	44/1376=3.2 ± 0.47	175/3052=5.7 ± 0.42

[1] Each entry contains two results: the upper one is for all complex structures ± S,D. error, and the lower one is for all complex structures ± relative error that pass a 40% sequence identity cutoff to minimize redundancy within protein families. S.D. is calculated assuming a binomial distribution.

Table S3.

Analysis of Phosphotheft Motif Among Hetero-oligomers on a per residue basis[1]

Parameter[1]	Invertebrates	Vertebrates	Human	All
S/T anywhere but not at interface	2571447/ 21643739=11.9	1487175/ 10611252=14.0	998990/ 6811633=14.7	4058622/ 32254991=12.6
(normalized to total number of residues; not at interface in all complexes)	1799382/ 14924935=12.1	1194373/ 8402776=14.2	843368/ 5648894=14.9	2993755/ 23327711=12.8
S/T anywhere on surface	121342/ 1043735=11.6	109288/ 764972=14.3	85265/ 587353=14.5	230630/ 1808707=12.8
(Residue)	77031/ 667512=11.5	78634/ 551258=14.3	64087/ 435144=14.7	155665/ 1218770=12.8
S/T anywhere on interface	11276/ 90025=12.5	7149/ 49736=14.4	4783/ 35979=13.3	18425/ 139761=13.2
(Residue)	6636/ 53131=12.5	5323/ 36736=14.5	3585/ 26699=13.4	11959/ 89867=13.3
R/K anywhere but not at interface	2249948/ 21643739=10.4	1086342/ 10611252=10.2	718216/ 6811633=10.5	3336290/ 32254991=10.3
(Residue)	1550733/ 14924935=10.4	857682/ 8402776=10.2	593357/ 5648894=10.5	2408415/ 23327711=10.3
R/K anywhere on surface	194023/ 1043735=18.6	142649/ 764972=18.6	110973/ 587353=18.9	336672/ 1808707=18.6
(Residue)	126232/ 667512=18.9	102391/ 551258=18.6	81832/ 435144=18.8	228623/ 1218770=18.8
R/K anywhere on interface	22285/ 90025=24.8	11298/ 49736=22.7	8037/ 35979=22.3	33583/ 139761=24.0
(Residue)	13191/ 53131=24.8	8316/ 36736=22.6	6011/ 26699=22.5	21507/ 89867=23.9
D/E anywhere but not at interface	2589417/ 21643739=12.0	1169997/ 10611252=11.0	788140/ 6811633=11.6	3759414/ 32254991=11.7
(Residue)	1799721/ 14924935=12.1	928233/ 8402776=11.0	649706/ 5648894=11.5	2727954/ 23327711=11.7
D/E anywhere on surface	204152/ 1043735=19.6	138772/ 764972=18.1	109378/ 587353=18.6	342924/ 1808707=19.0
(Residue)	133400/ 667512=20.0	100335/ 551258=18.2	80594/ 435144=18.5	233735/ 1218770=19.2
D/E anywhere on interface	27402/ 90025=30.4	14744/ 49736=29.6	10481/ 35979=29.1	42146/ 139761=30.2
(Residue)	16379/ 53131=30.8	10761 36736=29.3	7639/ 26699=28.6	27140/ 89867=30.2

[1] Each entry contains two results: the upper one is for all individual residues within the complex, while the lower one is for all individual residues within the complex that pass a 40% sequence identity cutoff to minimize redundancy within protein families.

Table S4. PEBP species exhibiting conservation of S153 *Homo sapiens*

Pan troglodytes
Gorilla gorilla
Callithrix jacchus
Pongo abelii
Chlorocebus sabaeus
Macaca mulatta
Macaca fascicularis
Papio anubis
Tupaia chinensis
Loxodonta africana
Bos taurus
Felis catus
Ovis aries
Mustela putorius furo
Ailuropoda melanoleuca
Sus scrofa
Otolemur garnettii
Equus caballus
Cavia porcellus
Desmodus rotundus
Canis lupus familiaris
Myotis lucifugus
Neovison vison
Camelus ferus
Rattus norvegicus
Nipponia nippon
Chaetura pelagica
Alligator mississippiensis
Amazona aestiva
Nomascus leucogenys
Aptenodytes forsteri
Picoides pubescens
Oreochromis niloticus
Gasterosteus aculeatus
Larimichthys crocea
Takifugu rubripes
Myotis brandtii
Xenopus laevis

Xenopus tropicalis
Astyanax mexicanus
Danio rerio
Pygoscelis adeliae
Pipa carvalhoi
Pelecanus crispus
Calypte anna

Table S5. Bax species exhibiting conservation of phosphotheft motif *Homo sapiens*

Macaca fascicularis
Chlorocebus sabaeus
Macaca mulatta
Otolemur garnettii
Bos mutus
Mustela putorius furo
Capra hircus
Bos taurus
Canis lupus familiaris
Ictidomys tridecemlineatus
Sus scrofa
Felis catus
Callithrix jacchus
Papio anubis
Ailuropoda melanoleuca
Gorilla gorilla gorilla
Heterocephalus glaber
Cavia porcellus
Pteropus alecto
Rattus norvegicus
Ovis aries
Mus musculus
Cricetulus griseus
Oryctolagus cuniculus
Tupaia chinensis
Camelus ferus
Monodelphis domestica
Fukomys damarensis
Pongo abelii
Myotis lucifugus
Pan troglodytes
Nomascus leucogenys
Loxodonta africana
Bubalus bubalis
Mesocricetus auratus
Equus caballus
Alligator mississippiensis
Anolis carolinensis

Xenopus tropicalis
Myotis davidii
Xenopus laevis
Taeniopygia guttata

Table S6. EEA1 species exhibiting conservation of phosphotheft motif *Homo sapiens*

Sarcophilus harrisii
Equus caballus
Bos mutus
Gorilla gorilla gorilla
Mustela putorius furo
Papio anubis
Pongo abelii
Oryctolagus cuniculus
Neovison vison
Felis catus
Macaca fascicularis
Macaca mulatta
Nomascus leucogenys
Chlorocebus sabaeus
Pan troglodytes
Otolemur garnettii
Callithrix jacchus
Ictidomys tridecemlineatus
Pteropus alecto
Sus scrofa
Loxodonta africana
Heterocephalus glaber
Cricetulus griseus
Tupaia chinensis
Myotis davidii
Fukomys damarensis
Desmodus rotundus
Canis lupus familiaris
Rattus norvegicus
Ailuropoda melanoleuca
Ovis aries
Ornithorhynchus anatinus
Fulmarus glacialis
Myotis lucifugus
Myotis brandtii
Mus musculus
Monodelphis domestica
Cavia porcellus

Alligator mississippiensis
Phaethon lepturus
Phalacrocorax carbo
Gallus gallus
Meleagris gallopavo
Eurypyga helias
Pterocles gutturalis
Pygoscelis adeliae
Cathartes aura
Mesitornis unicolor
Tyto alba
Calypte anna
Anas platyrhynchos
Pelecanus crispus
Nestor notabilis
Ficedula albicollis
Taeniopygia guttata
Nipponia nippon
Pelodiscus sinensis
Amazona aestiva
Balearica regulorum gibbericeps
Manacus vitellinus
Egretta garzetta
Aptenodytes forsteri
Chlamydotis macqueenii
Cuculus canorus
Tinamus guttatus
Opisthocomus hoazin
Struthio camelus australis
Danio rerio
Podiceps cristatus
Acanthisitta chloris
Charadrius vociferus
Ophiophagus hannah
Crotalus horridus
Anolis carolinensis
Lepisosteus oculatus
Latimeria chalumnae
Astyanax mexicanus
Larimichthys crocea

Takifugu rubripes
Oryzias latipes
Gasterosteus aculeatus
Tetraodon nigroviridis
Poecilia formosa
Xiphophorus maculatus
Scleropages formosus
Fundulus heteroclitus
Ictalurus punctatus
Oreochromis niloticus
Oncorhynchus mykiss
Xenopus tropicalis
Callorhinchus milii

Table S7. Troponin I species exhibiting conservation of phosphotheft motif *Homo sapiens*
Nomascus leucogenys
Pongo abelii
Chlorocebus sabaeus
Pan troglodytes
Macaca fascicularis
Macaca mulatta
Callithrix jacchus
Canis lupus familiaris
Sus scrofa
Ailuropoda melanoleuca
Mustela putorius furo
Cavia porcellus
Felis catus
Ictidomys tridecemlineatus
Mus musculus
Heterocephalus glaber
Rattus norvegicus
Otolemur garnettii
Oryctolagus cuniculus
Tupaia chinensis
Bos taurus
Bos mutus
Ovis aries
Equus caballus
Capra hircus
Papio anubis
Neovison vison
Monodelphis domestica
Anolis carolinensis
Rhinella marina
Xenopus laevis
Alligator mississippiensis
Xenopus tropicalis
Lithobates catesbeiana
Latimeria chalumnae
Meleagris gallopavo

Gallus gallus
Coturnix coturnix japonica
Gorilla gorilla gorilla
Lepisosteus oculatus
Ophiophagus hannah
Danio rerio
Callorhinchus milii
Oncorhynchus mykiss
Esox lucius
Anas platyrhynchos
Picoides pubescens
Sarcophilus harrisii
Salmo salar
Ficedula albicollis
Gasterosteus aculeatus
Balearica regulorum gibbericeps
Cathartes aura
Egretta garzetta
Haliaeetus albicilla
Tinamus guttatus
Cuculus canorus
Loxodonta africana
Coturnix coturnix
Fukomys damarensis
Tauraco erythrolophus
Fulmarus glacialis
Gavia stellata
Manacus vitellinus
Phoenicopterus ruber ruber
Nipponia nippon
Charadrius vociferus
Pygoscelis adeliae
Tyto alba
Corvus brachyrhynchos
Pelecanus crispus
Podiceps cristatus
Taeniopygia guttata
Pelodiscus sinensis

Buceros rhinoceros silvestris
Struthio camelus australis
Phalacrocorax carbo
Astyanax mexicanus
Oreochromis niloticus
Opisthocomus hoazin
Nestor notabilis
Fundulus heteroclitus
Scleropages formosus
Dicentrarchus labrax
Camelus ferus
Poecilia formosa
Xiphophorus maculatus
Oryzias latipes
Takifugu rubripes
Tetraodon nigroviridis
Poeciliopsis prolifica
Ictalurus punctatus
Larimichthys crocea
Myotis davidii
Amazona aestiva
Anoplopoma fimbria
Pelodytes ibericus
Ictalurus furcatus
Antrostomus carolinensis
Halocynthia roretzi
Ciona intestinalis
Campylomormyrus compressirostris
Ciona savignyi
Polyandrocarpa misakiensis
Chelyosoma siboja
Phaethon lepturus
Merops nubicus
Pimephales promelas
Clupea harengus